Proton mean field in ^{40}Ca between -60 MeV and $+200$ MeV deduced from a dispersive optical-model analysis

W. Tornow and Z. P. Chen*
Department of Physics, Duke University, Durham, North Carolina 27706
and Triangle Universities Nuclear Laboratory, Duke Station, Durham, North Carolina 27706

J. P. Delaroche
Service de Physique et Techniques Nucléaires, Centre d'Études de Bruyères-le-Châtel, F-91680 Bruyères le-Châtel, France
and Triangle Universities Nuclear Laboratory, Duke Station, Durham, North Carolina 27706
(Received 26 March 1990)

The p-^{40}Ca mean field is derived from an optical-model (OM) analysis that explicitly incorporates the dispersion relation connecting the real and imaginary parts of the mean field. This analysis is based on differential cross-section, analyzing power, and reaction cross-section data available in the energy range between 20 and 180 MeV. The extrapolation of the OM potential from positive to negative energies provides the shell-model potential. This extrapolation is guided by known single-particle energies. The deeply bound $1p$ and $1s$ orbits clearly indicate the need for a linear rather than an exponential energy dependence of the Hartree-Fock potential at large negative energies. The analysis also provides root-mean-square radii, occupation probabilities, spectral functions, and absolute spectroscopic factors for proton single-particle orbits in ^{40}Ca. Our calculated 15% depletion of the hole states in ^{40}Ca is lower than that suggested for ^{208}Pb from theoretical and experimental studies. We also find that a substantial amount of single-particle strength in ^{40}Ca is located at rather high excitation energy.

I. INTRODUCTION

During the past few years model studies of neutron and proton elastic scattering at low incident energies (i.e., $E \leq 100$ MeV) from medium to heavy nuclei have enjoyed renewed interest. The rationale behind this revival is related to the fact that elastic scattering data are well suited to guide the extrapolation of the empirical, complex optical-model potential (OMP) towards bound-state energies. In this negative energy regime, the real part of the OMP is usually called the shell-model potential. As shown by Mahaux and Ngô,[1] the extrapolation of the nucleon-nucleus potentials from positive to negative energies is based on the dispersion relation (DR) which connects the real and imaginary OMP components. This method, designed to derive nucleon mean fields in closed—or nearly closed—shell nuclei, is usually referred to as the dispersive optical-model analysis (DOMA). It has been successfully applied in the study of neutron scattering data and/or single-particle (s.p.) bound-state properties for ^{40}Ca (Refs. 2-4), ^{51}V (Ref. 5), ^{86}Kr (Ref. 6), ^{90}Zr (Ref. 7), ^{93}Nb (Ref. 8), ^{208}Pb (Refs. 9 and 10), and ^{209}Bi (Ref. 11). Simultaneously, an alternate method referred to as the iterative moment approach (IMA) has also been used to study the neutron mean field in ^{40}Ca (Ref. 12), ^{89}Y (Ref. 13), and ^{208}Pb (Ref. 14) and the proton mean field in ^{40}Ca (Ref. 12) and ^{208}Pb (Refs. 15 and 16).

Since the DOMA approach has not been used thoroughly in proton-nucleus mean field studies, we have found it important to apply this method for the p-^{40}Ca system. The ^{40}Ca nucleus is likely to be a better choice than ^{208}Pb, another testing ground often considered for OMP studies, because its Coulomb barrier is lower. This feature should help to avoid problems that apparently obscured a recent p-^{208}Pb analysis.[10] Our study of the p-^{40}Ca system also offers the opportunity to investigate whether an imaginary spin-orbit (SO) interaction is needed to describe the available analyzing power [$A_y(\theta)$] data. This component of the SO interaction was found to be negligible in DOMA studies of $A_y(\theta)$ data for polarized neutron scattering off ^{40}Ca,[2] while conventional analyses consistently required a positive imaginary SO potential.[17]

The proton data set used in the present study is specified in Table I. It includes differential cross-section [$\sigma(\theta)$], reaction cross-section (σ_R), and $A_y(\theta)$ data collected in the energy range $E=20-180$ MeV. The $\sigma(\theta)$ and $A_y(\theta)$ measurements available below 20 MeV have been ignored in building the dispersive OM potential, since nuclear structure effects and compound nuclear processes tend to obscure the analysis, as pointed out by Van Oers.[33] As is well known, the data considered above 100 MeV are successfully described in the framework of the Dirac phenomenology (DP) using wine-bottle bottom, real central potentials.[34] The present study offers the opportunity to compare these DP results with DOMA predictions at the higher incident energies under consideration.

The paper is organized as follows. Section II is devot-

 ©1990 The American Physical Society

TABLE I. Reference list for the elastic p-^{40}Ca data considered in the standard OMP analysis. The symbol x attached to either $\sigma(\theta)$ or $A_y(\theta)$ means that data exist for the observable at a specific incident energy. The references for the p-^{40}Ca reaction cross-section data are summarized in Ref. 32.

E (MeV)	$\sigma(\theta)$	$A_y(\theta)$	Reference
19.6	x		18
21.0	x	x	18,19
26.3	x	x	19,20
30.3	x	x	21,22
34.8	x		23
40.0	x	x	24
45.5	x	x	25
48.0	x		19
49.0		x	26
61.4	x		27
65.0	x	x	28,29
80.2	x	x	30,31

ed to the DOMA at positive energies. In Sec. III we present our results obtained for the bound and quasi-bound single-particle energies, effective masses, root-mean-square radii, occupation probabilities, absolute spectroscopic factors, and spectral functions, and show comparisons with available experimental information. Section IV compares some of our results with the IMA results of Mahaux and Sartor.[12] Finally, Sec. V summarizes our results.

II. PROTON-^{40}Ca MEAN FIELD AT POSITIVE ENERGIES

Any reliable determination of the nuclear mean field requires a "complete" set of experimental data over a broad energy range. It is especially important to place constraints on the high-energy behavior of the absorptive potential. As can be seen from Table I, these conditions are met for the p-^{40}Ca system. We have not considered the $\sigma(\theta)$ and $A_y(\theta)$ data available between 200 MeV and 1 GeV, since it is well known that the Schrödinger phenomenology, as used in the present work, is not considered to be appropriate for describing scattering data in the intermediate energy range.

In the Schrödinger equation, the proton OMP $\mathcal{U}(r,E)$ for ^{40}Ca is defined as

$$\begin{aligned}\mathcal{U}(r,E)=&-\mathcal{V}(r,E)-iW_V(E)f(r,R_W,a_W)\\&+4ia_D W_D(E)\frac{d}{dr}f(r,R_D,a_D)\\&+2\chi_\pi^2[V_{\rm SO}(E)+iW_{\rm SO}(E)]\frac{1}{r}\frac{d}{dr}\\&\times f(r,R_{\rm SO},a_{\rm SO})+V_C(r)\ ,\end{aligned}\tag{1}$$

where

$$f(r,R_i,a_i)=[1+\exp(r-R_i)/a_i]^{-1}$$

is a Woods-Saxon (WS) form factor with $R_i=r_i A^{1/3}$ (fm), $V_C(r)$ the Coulomb potential (MeV), and E the incident energy (MeV). The functional form of the real central potential $\mathcal{V}(r,E)$ depends on the type of analysis. Since we have performed both standard OMP analysis and DOMA, $\mathcal{V}(r,E)$ is defined as (i) standard OMP analysis:

$$\mathcal{V}(r,E)=V(E)f(r,R_V,a_V)\ ,\tag{2}$$

and (ii) DOMA:

$$\mathcal{V}(r,E)=\mathcal{V}_{\rm HF}(r,E)+\Delta\mathcal{V}(r,E)\ ,\tag{3}$$

where

$$\mathcal{V}_{\rm HF}(r,E)=V_{\rm HF}(E)f(r,R_{\rm HF},a_{\rm HF})$$

is the so-called Hartree-Fock (HF) component of $\mathcal{V}(r,E)$. Its energy dependence is expected to be smooth in the energy range of interest. The second term in Eq. (3), $\Delta\mathcal{V}(r,E)$, is the DR contribution which is calculated from the imaginary part of the OMP as will be discussed in Sec. II B.

A. Standard optical-model analysis

In this section we briefly describe our standard OMP analysis. The study was performed using grid searches. This well-known technique, discussed for instance in Refs. 7 and 10, provides the information on geometries and energy dependences of the absorptive potential that is needed later to obtain the dispersive contribution $\Delta\mathcal{V}(r,E)$. In that perspective, the standard OMP analysis represents the first stage of the DOMA described in Sec. II B. Relativistic kinematics was used throughout the present work.

The number of adjustable parameters in Eqs. (1) and (2) was reduced by imposing the constraint of identical geometries for the real and imaginary volume potentials:

$$r_V=r_W \text{ and } a_V=a_W\ .$$

In the early stage of our studies it was observed that the surface absorption W_D at very low energies increases rapidly with increasing energy and then decreases smoothly beyond $E\sim 30$ MeV. This energy dependence can conveniently be described by the damped Jeukenne and Mahaux form[35,7]

$$W_D(E)=a\frac{(E-E_F)^4}{(E-E_F)^4+b^4}\exp[-c(E-E_F)]\ \text{(MeV)}\tag{4}$$

with $a=8.4$ MeV, $b=15$ MeV, and $c=0.011$ MeV^{-1}, and with $E_F=-4.71$ MeV as the Fermi energy. This parametrization is valid only for energies up to 80 MeV because the available $\sigma(\theta)$ and $A_y(\theta)$ data beyond this energy have not been considered at this stage of the analysis.

For the volume absorption W_V, the Jeukenne and Mahaux form[35] was used:

$$W_V(E)=a'\frac{(E-E_F)^4}{(E-E_F)^4+(b')^4}\ \text{(MeV)}\tag{5}$$

with $a'=12.4$ MeV and $b'=70.3$ MeV.

The depth $V_{\rm SO}$ of the real SO potential was found to be slightly energy-dependent:

$$V_{SO}(E)=5.6-0.008E \text{ (MeV)} . \quad (6)$$

A very small negative imaginary component W_{SO} (MeV) was necessary for fine tuning the fits to the $A_y(\theta)$ data only for energies above 50 MeV:

$$W_{SO}(E)=0, \quad E \leq 50 \text{ MeV} ,$$
$$W_{SO}(E)=-(E-50)/180, \quad E>50 \text{ MeV} . \quad (7)$$

A linear energy dependence was found for the real central potential strength $V(E)$:

$$V(E)=49.80-0.19(E-E_F) \text{ (MeV)} . \quad (8)$$

Finally, in the energy range between 20 and 80 MeV, the potential form factors were energy independent. The following values were obtained: (i) volume central potentials,

$$r_V=r_W=1.20 \text{ fm and } a_V=a_W=0.73 \text{ fm} ;$$

(ii) surface absorptive potential,

$$r_D=1.26 \text{ fm and } a_D=0.62 \text{ fm} ; \quad (9)$$

(iii) spin-orbit potentials,

$$r_{SO}=1.05 \text{ fm and } a_{SO}=0.58 \text{ fm} ;$$

and (iv) Coulomb radius,[36,12]

$$r_C=1.314 \text{ fm} .$$

For each geometric parameter, the grid search method provides a range of values for which the fits remain within "limits of acceptability." For instance, the overall quality of the OMP fits shown in Fig. 1 as solid lines is preserved as long as the values for r_V and a_V fall in the interval $1.18 \leq r_V \leq 1.22$ fm and $0.72 \leq a_V \leq 0.74$ fm, respectively. For unknown reasons, the radial shape of the real central potential cannot be determined more precisely in this spherical OMP analysis, a feature which was also observed in earlier, independent coupled-channel studies of neutron and proton scattering off ^{40}Ca.[17] Furthermore, we have found no clear evidence for a systematic decrease of r_V with increasing energy in the 20–80 MeV energy range. This is the reason why an energy-independent value was assigned for r_V in Eq. (9).

The solid curves shown in Fig. 1 for $\sigma(\theta)$ [Fig. 1(a)] and $A_y(\theta)$ [Fig. 1(b)] were obtained using Eqs. (1) and (2) along with the parameters specified in Eqs. (4)–(9). Considering the large energy range investigated and the constraints imposed on the OMP, the overall agreement between this spherical, "fixed geometry" OMP analysis and the $\sigma(\theta)$ and $A_y(\theta)$ data is very satisfactory.

B. Dispersive optical-model analysis

The dispersive correction $\Delta\mathcal{V}(r,E)$ which links the real and imaginary components of the OMP is usually defined by

$$\Delta\mathcal{V}_i(r,E)=\frac{P}{\pi}\int_{-\infty}^{+\infty}\frac{\mathcal{W}_i(r,E)}{E'-E}dE' , \quad (10)$$

where P indicates a principal value and $i=(V,D)$ refers to either the volume or surface absorptive potential. With these notations, $\Delta\mathcal{V}(r,E)$ of Eq. (3) can be expressed

$$\Delta\mathcal{V}(r,E)=\Delta\mathcal{V}_V(r,E)+\Delta\mathcal{V}_D(r,E) , \quad (11)$$

with

$$\Delta\mathcal{V}_V(r,E)=\Delta V_V(E)f(r,R_V,a_V) ,$$

and (12)

$$\Delta\mathcal{V}_D(r,E)=-4a_D\Delta V_D(E)\frac{d}{dr}f(r,R_D,a_D) .$$

The evaluation of $\Delta\mathcal{V}(r,E)$ requires the knowledge of the absorptive potentials in the entire energy range from $-\infty$ to $+\infty$. In practice, this condition cannot be fulfilled since phenomenological OMP analyses at the most provide $\mathcal{W}(r,E)$ only up to a few hundred MeV. As mentioned already earlier, for p-^{40}Ca, $\sigma(\theta)$ and $A_y(\theta)$ data are available up to about 1000 MeV. Since the validity of the Schrödinger approach to nucleon scattering has proven to be doubtful in the intermediate energy range, the highest possible energy at which $\mathcal{W}(r,E)$ could reasonably be anchored is $E=182$ MeV. Only a few $\sigma(\theta)$ and $A_y(\theta)$ data exist in the energy range $E=80$–182 Mev.[30,31,37] These data were used to extend the parametrization of $W_D(E)$ from $E=80$ MeV up to infinity. A reasonable OMP description of the data is achieved with the OMP parameters from Sec. II A, provided that $W_D(E)$ be linearly extrapolated beyond 80 MeV. Thus, $W_D(E)$ is defined through Eq. (4) for $E \leq 80$ MeV, and

$$W_D(E)=4.27-0.011(E-E_F) \text{ (MeV)} \quad (13)$$

above 80 MeV until it reaches zero at $E=390$ MeV. Note that both parametrizations have the same slope at $E=80$ MeV. The need for an imaginary surface absorption at intermediate energies has also been indicated in a recent Dirac optical-model analysis.[38]

The continuation of $\mathcal{W}(r,E)$ to negative energies lower than E_F is usually accomplished by assuming that the absorption is symmetric around the Fermi energy E_F:

$$\mathcal{W}(r,E_F+E)=\mathcal{W}(r,E_F-E) .$$

As a consequence, the DR terms are skew-symmetric with respect to E_F:

$$\Delta\mathcal{V}_i(r,E_F+E)=-\Delta\mathcal{V}_i(r,E_F-E) .$$

The DR terms were evaluated using the relation

$$\Delta\mathcal{V}_i(r,E)=\frac{2}{\pi}(E-E_F)P\int_{E_F}^{\infty}\frac{\mathcal{W}_i(r,E')}{(E'-E_F)^2-(E-E_F)^2}\times dE' . \quad (14)$$

Figure 2 presents the potential depths W_D and W_V as well as the corresponding DR terms ΔV_D and ΔV_V as functions of $(E-E_F)$ in the energy range from −75 MeV to +200 MeV. As can be seen, the surface dispersive term ΔV_D crosses through zero at $(E-E_F)=33.7$ MeV.

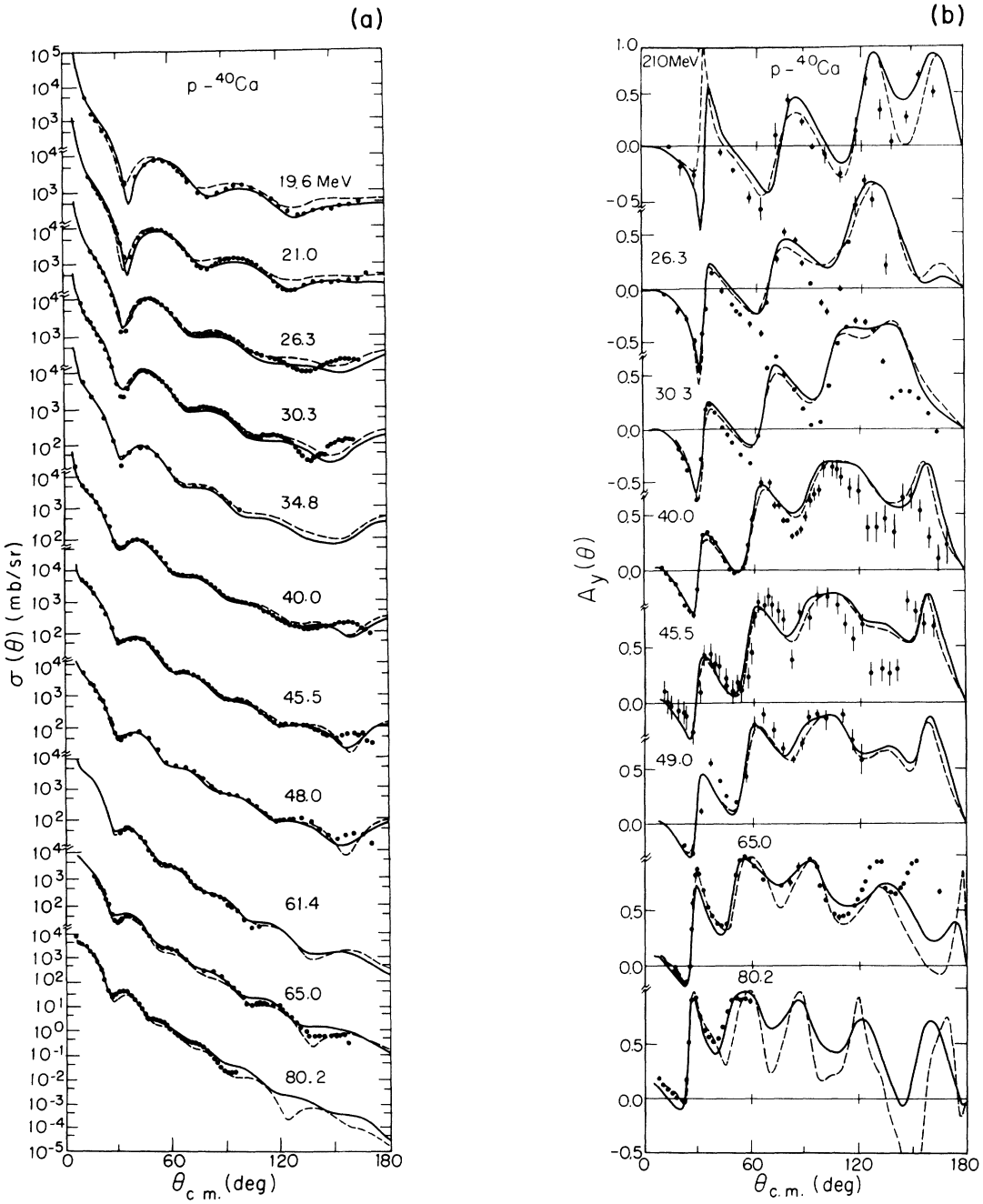

FIG. 1. Comparison between spherical optical-model calculations and p-^{40}Ca elastic differential cross-section (a) and analyzing power (b) data. References to the measurements are given in Table I. The solid curves represent standard OMP analyses based on the geometries and energy dependences given in Sec. II A in functional form. The dashed curves display the results of the dispersive optical-model analysis (DOMA) discussed in Sec. II B. Here the potential defined by Eqs. (17)–(19) was used.

Once the values for the depths and geometries of the absorptive and spin-orbit potentials as well as those for the DR components of the mean field have been fixed, the only potential that remains to be determined is the empirical Hartree-Fock term $\mathcal{V}_{\rm HF}(r,E)$ [see Eq. (3)]. Again, as in Sec. II A, we have found it difficult to obtain a well-defined optimum geometry for this volume potential. Even though we could not rule out the possibility for a slight energy dependence of its radial shape, a fixed geometry was assumed in order to reduce the number of free parameters. The optimum values found for the radius and diffuseness of the HF field are

$$r_{\rm HF}=1.20 \text{ fm and } a_{\rm HF}=0.73 \text{ fm} , \quad (15)$$

respectively. The empirical values obtained for the strength $V_{\rm HF}$ of the HF potential in the 20–80 MeV en-

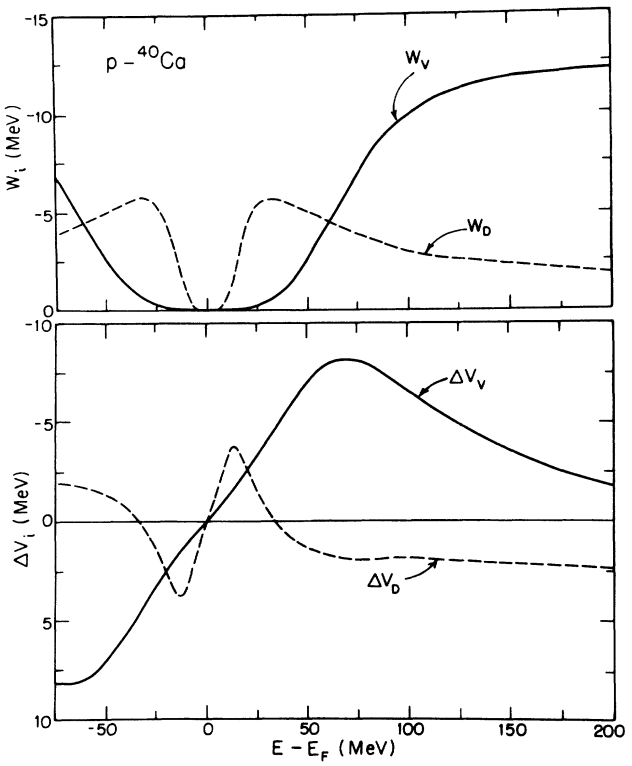

FIG. 2. Absorptive potentials and dispersive correction terms for p-^{40}Ca. The solid curves represent the energy dependence of the volume absorption W_V (top panel) and the volume dispersive correction term ΔV_V (bottom panel) as function of the shifted energy $(E-E_F)$. Here E is the incident energy and E_F is the Fermi energy of a proton in ^{40}Ca ($E_F=-4.71$ MeV). The dashed curves display the energy dependence of the surface absorption W_D (top panel) and the surface dispersive correction ΔV_D (bottom panel).

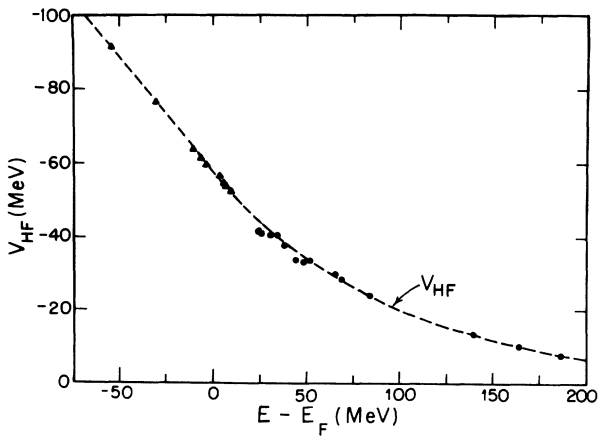

FIG. 3. Energy dependence of the depth of the empirical Hartree-Fock potential for p-^{40}Ca. The dots and triangles represent results obtained from the DOMA that best describes the scattering data and bound-state energies, respectively. The dashed curve was calculated using Eqs. (17)–(19).

ergy range are shown as dots in Fig. 3. These values follow a smooth pattern (dashed curve in Fig. 3) which will be discussed in Sec. III.

The dashed curves shown in Fig. 1 represent the DOMA results for energies up to 80 MeV. As can be seen, a good overall agreement between data and calculations is achieved. Below 50 MeV, the fits to the $A_y(\theta)$ data do not require an imaginary SO potential. This observation, deduced from polarized proton scattering, is in agreement with that obtained from polarized neutron scattering.[2] For $E>50$ MeV, only a small amount of imaginary SO potential strength is needed [see Eq. (7)]. W_{SO} could also have been set equal to zero without spoiling the quality of the fits. Our results are consistent with the nuclear structure calculations of Brieva and Rook[39] for the imaginary spin-orbit potential depth.

The DOMA analysis was extended beyond 80 MeV using a smooth extrapolation of V_{HF} (see Fig. 3) up to $E=200$ MeV. Results are shown at $E=135$, 162, and 182 MeV in Fig. 4, where they are compared with experimental information. As can be seen, the DOMA provides a rather good description of the $\sigma(\theta)$ and $A_y(\theta)$ data, in particular at $E=182$ MeV. At this incident energy, the quality of the fits is comparable to that obtained with DP.[34] Here, like at any other lower incident energy, the DOMA potential includes surface and volume components which sum up to form the volume shape shown as a solid curve in Fig. 5. This radial shape is at variance with predictions from both DP (dashed curve) and from nonrelativistic Brueckner-Hartree-Fock (BHF) mean-field theory (dotted curve, taken from Fig. 26 in Ref. 40).

The DOMA has also been used to predict reaction

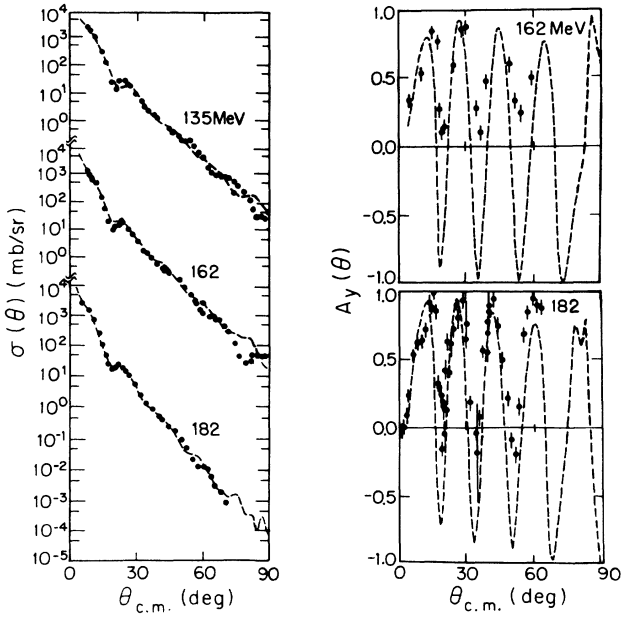

FIG. 4. Comparison between DOMA and $\sigma(\theta)$ (left side) and $A_y(\theta)$ (right side) data at 135, 162, and 182 MeV (from Refs. 30, 31, and 37). Here the HF potential represented by the dashed curve in Fig. 3 was used together with the absorptive potentials and the dispersive terms displayed in Fig. 2.

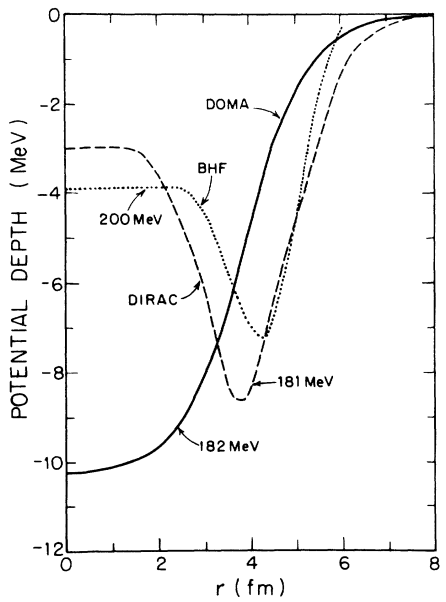

FIG. 5. Radial shape of the real central potential near 200 MeV. Comparison between the present DOMA result (solid curve) and those obtained from Dirac phenomenology (dashed curve) and nonrelativistic Brueckner-Hartree-Fock mean-field theory (dotted curve).

cross sections σ_R for which some data are available from 10 to 182 MeV. The comparison between data[32] and calculations is shown in Fig. 6. Except near 100 MeV, the agreement is generally good. Obviously, more σ_R data between 50 and 200 MeV are required to validate this comparison. At the low-energy end, the calculations slightly overpredict the measurements. This might indicate the need for incorporating angular momentum dependent terms in the analysis, as suggested in earlier phonomenological studies at low energy[4] and recent microscopic calculations.[41]

III. PROTON-^{40}Ca MEAN FIELD AT BOUND- AND QUASIBOUND-STATE ENERGIES

We now present an extrapolation of the mean field derived in Sec. II B towards negative energies. This exercise provides a sensitive test for the parametrizations of the absorptive and HF potentials at positive energies.

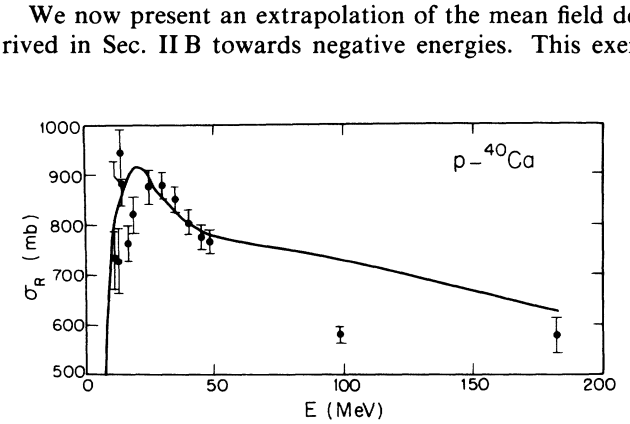

FIG. 6. Comparison between DOMA predictions and reaction cross-section data for p-^{40}Ca (Ref. 32).

The extrapolation towards the bound-state region requires experimental information about the single-particle energies on both sides of the Fermi energy E_F. In Fig. 7 the column at the center represents the experimental s.p. centroid energies quoted in Ref. 12 for the particle (i.e., $E_{nlj} > E_F$) and hole (i.e., $E_{nlj} < E_F$) states with quantum numbers (n,l,j). The HF potential strength at $E = E_F = -4.71$ MeV was determined in such a way that the calculated energies for the first-particle state ($1f_{7/2}$) and the first-hole state ($1d_{3/2}$) are approximately symmetric around the Fermi energy. This requirement provides the value of the HF potential depth

$$V_{\rm HF}(E_F) = -58.25 \text{ MeV} , \tag{16}$$

which was used as an anchor point in the determination of the energy dependence of $V_{\rm HF}$ from -60 MeV up to $+200$ MeV. This energy dependence is discussed in the following section.

A. Single-particle and single-hole state energies

It would be convenient to parametrize the energy dependence of $V_{\rm HF}$ at both positive and negative energies using the simple functional form[9]

$$V_{\rm HF}(E) = V_{\rm HF}(E_F)\exp[-\alpha(E-E_F)/V_{\rm HF}(E_F)] . \tag{17}$$

However, this parametrization predicts hole states that generally are too tightly bound. Therefore, a linear ener-

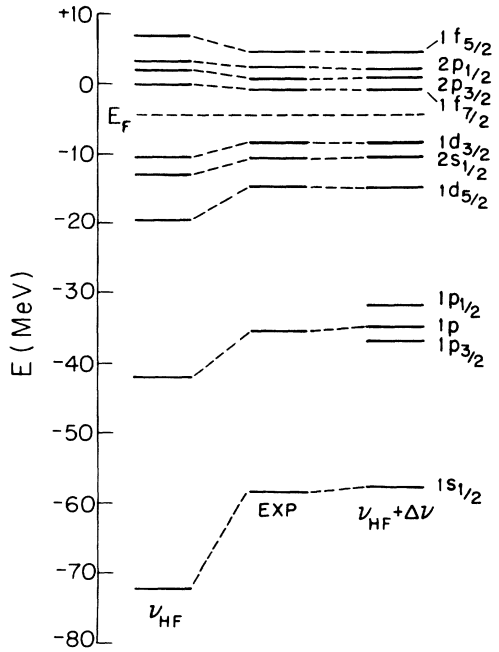

FIG. 7. Proton single-particle energies E_{nlj} in ^{40}Ca. The column labeled EXP represents experimental values as compiled in Ref. 12. The columns labeled $\mathcal{V}_{\rm HF}$ and $\mathcal{V}_{\rm HF}+\Delta\mathcal{V}$ give the energies obtained from the Hartreee-Fock potential and from the real part of the full mean field, respectively.

gy dependence is preferred for $V_{\rm HF}$ in the region $E<E_F$:

$$V_{\rm HF}(E)=V_{\rm HF}(E_F)-\alpha(E-E_F)\ . \tag{18}$$

According to Ref. 4, this behavior reflects the fact that the energy dependence of $V_{\rm HF}(E)$ is due to the nonlocality of the actual Hartree-Fock field. With $\alpha=0.616$, a value that is large, but comparable in magnitude with those determined in Refs. 4 and 12, Eqs. (17) and (18) yield a smooth energy dependence of $V_{\rm HF}$ (see dashed curve in Fig. 3) and provide an excellent overall representation of the optimum individual $V_{\rm HF}$ values obtained at both positive (dots) and negative energies (triangles). These equations are also used to produce the dashed curves shown in Figs. 1 and 4, and the solid curve in Fig. 6.

The calculated energies E_{nlj} for the s.p. states are shown on the right-hand side (third column) of Fig. 7. Here we used the real part of the full mean field, i.e.,

$$\mathcal{V}(r,E)=\mathcal{V}_{\rm HF}(r,E)+\Delta\mathcal{V}_V(r,E)+\Delta\mathcal{V}_D(r,E) \tag{19}$$

defined by Eqs. (3), (9), and (11), and the spin-orbit potential given by Eqs. (6) and (9). The calculated s.p. energies compare very well with the experimental data (second column). As known from Refs. 9 and 12, the inclusion of the dispersive terms $\Delta\mathcal{V}_V$ and $\Delta\mathcal{V}_D$ yields higher level densities than do mean-field calculations that ignore these terms. This is illustrated in Fig. 7, where the first column represents the level scheme calculated with the dispersive terms turned off.

B. Other bound-state properties

The dispersion relation approach to the nuclear mean field also provides information about the effective masses, s.p. wave functions, occupation probabilities, absolute spectroscopic factors, and spectral functions. Some of these quantities can be determined experimentally, in particular using electron beams. In this respect, the continuous electron beam accelerators, like those under construction at Mainz (MAMI II) and Newport News (CEBAF), might provide valuable experimental information in the future. Predictions for these quantities are presented below.

1. *Effective masses*

For later calculations, we introduce three effective masses.[9] The mass $m^*(r,E)$ describes the energy dependence of the real part of the full mean field; it is defined as

$$m^*(r,E)/m=1-\frac{d}{dE}\mathcal{V}(r,E)\ . \tag{20}$$

In the Hartree-Fock approximation, the effective mass (i.e. k mass) reduces to $m^*_{\rm HF}(r,E)$ with

$$m^*_{\rm HF}(r,E)/m=1-\frac{d}{dE}\mathcal{V}_{\rm HF}(r,E)\ . \tag{21}$$

In the absence of dispersive terms the effective masses $m^*(r,E)$ and $m^*_{\rm HF}(r,E)$ are identical. Finally, the E mass is given as

$$\overline{m}(r,E)/m=1-\frac{d}{dE}\Delta\mathcal{V}(r,E)\ . \tag{22}$$

The radial dependence of the Hartree-Fock effective mass ratio $m^*_{\rm HF}(r,E)/m$ at $E=E_F$ is shown in Fig. 8 as a dashed curve. At the nuclear center, $m^*_{\rm HF}(r,E)/m$ takes on a value close to 0.4. The dashed-dotted curve represents the E mass, which exhibits a peak at the nuclear surface. The radial dependence of the full effective mass ratio $m^*(r,E)/m$ is given by the solid curve. At the nuclear center, its value is about 30% larger than that obtained with the Hartree-Fock potential. Due to the dispersive contribution, $m^*(r,E)/m$ exhibits a peak near the nuclear surface.

2. *Root-mean-square radii*

Following the notations and definitions given in Ref. 4, the rms radii were calculated as

$$R^{\rm rms}_{nlj}=\left[\int_0^\infty \bar{u}^2_{nlj}(r)r^2dr\right]^{1/2}\ . \tag{23}$$

The results obtained for the s.p. orbits in ^{40}Ca for $E<0$ are given in Table II together with the corresponding s.p. energies. Our calculated radii follow the pattern found in Ref. 4 for the neutron s.p. states in ^{40}Ca but are about 5% larger. In contrast with our findings, the radii given in Ref. 12 do not change much from one orbit to another. The very recent $(e,e'p)$ results for the $1d_{3/2}$ and $2s_{1/2}$ radii obtained by Kramer *et al.*[42] are in close agreement with the present calculations. It would be interesting to compare our predictions with experimental results for the deeply bound states.

3. *Occupation probabilities*

As shown by Mahaux and Ngô[43] and Mahaux and Sartor,[16] the occupation probability N_{nlj} for hole states ($E_{nlj}<E_F$) is approximately equal to

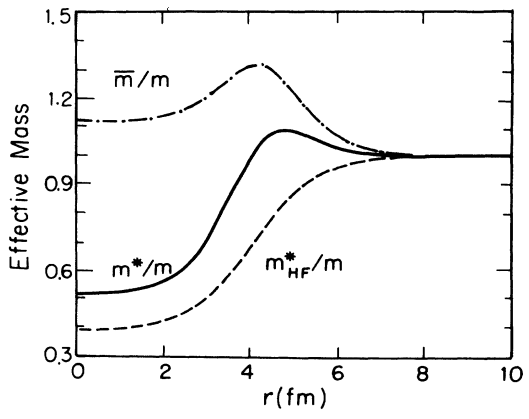

FIG. 8. Radial dependence of m^*/m (solid curve), $m^*_{\rm HF}/m$ (dashed curve), and $\overline{m}/m$ (dashed-dotted curve) at the Fermi energy. These quantities are defined by Eqs. (20)–(22).

TABLE II. Energy and root-mean-square radius of proton single-particle orbits in ^{40}Ca.

nlj	E_{nlj} (MeV)	R^{rms}_{nlj} (fm) Present work	Ref. 12	Ref. 42
$1f_{7/2}$	−1.15	4.31	4.07	
$1d_{3/2}$	−8.88	3.71	3.99	3.69(10)
$2s_{1/2}$	−10.67	3.87	3.96	3.72(10)
$1d_{5/2}$	−14.95	3.53	3.91	
$1p_{1/2}$	−31.62	2.94		
$1p_{3/2}$	−36.52	2.96		
$1s_{1/2}$	−57.38	2.33		

$$N_{nlj}=\int_0^\infty \bar{u}^{\,2}_{nlj}(r)\left[1+[m^*_{\rm HF}/m(r,E_{nlj})]^{-1}\pi^{-1}\times\int_{E_F}^{\infty}\frac{\mathcal{W}(r,E')}{(E'-E_{nlj})^2}dE'\right]dr\ , \tag{24}$$

while for particle states ($E_{nlj}>E_F$) N_{nlj} is given by

$$N_{nlj}=-\int_0^\infty \bar{u}^{\,2}_{nlj}(r)\left[[m^*_{\rm HF}/m(r,E_{nlj})]^{-1}\pi^{-1}\times\int_{-\infty}^{E_F}\frac{\mathcal{W}(r,E')}{(E'-E_{nlj})^2}dE'\right]dr\ . \tag{25}$$

The calculated probabilities for bound states are shown in Fig. 9 and listed in Table III, where they are compared with values deduced from $(e,e'p)$ (Refs. 44 and 45) and $(p,2p)$ (Ref. 46) measurements. The scatter which is seen among these experimental values (third through fifth columns) illustrates that the N_{nlj}'s are not very well determined. In contrast, our results clearly indicate a 15% depletion of the Fermi sea. This figure is reliable, provided that the calculated N_{nlj} values do not depend much on the assumption made for $\mathcal{W}(r,E)$ at large positive and negative energies.

TABLE III. Occupation probability of proton single-particle orbits in ^{40}Ca.

nlj	N_{nlj} Present work	$(e,e'p)$ Ref. 44	$(e,e'p)$ Ref. 45	$(p,2p)$ Ref. 46
$1f_{7/2}$	0.14			
$1d_{3/2}$	0.85	1.05	0.77[b]	0.5[b]
$2s_{1/2}$	0.87	1.0	0.65	0.25
$1d_{5/2}$	0.88	0.78	0.77[b]	0.5[b]
$1p_{1/2}$	0.91	1.7[a]	0.95[a]	1.0[a]
$1p_{3/2}$	0.92	1.7[a]	0.95[a]	1.0[a]
$1s_{1/2}$	0.93	1.85	0.75	>20

[a]Values are given for $1p$ and not individually for $1p_{1/2}$ and $1p_{3/2}$ states.
[b]Values are given for $1d$ and not individually for $1d_{3/2}$ and $1d_{5/2}$ states.

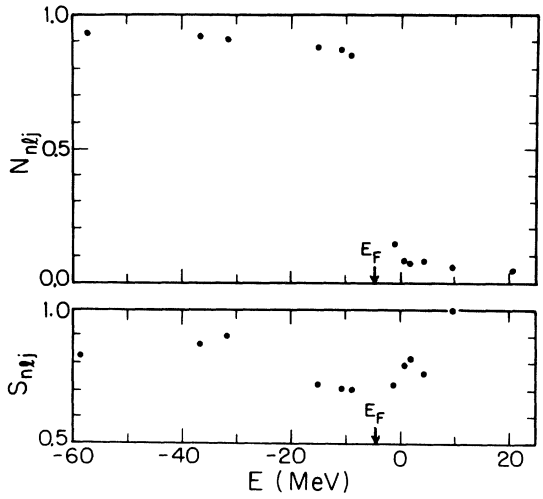

FIG. 9. Calculated occupation probability N_{nlj} (top panel) and spectroscopic factor S_{nlj} (bottom panel) of bound and quasi-bound single-particle states in ^{40}Ca.

4. *Spectroscopic factors*

The absolute spectroscopic factor is defined as follows:[16]

$$S_{nlj}=\int_0^\infty \bar{u}^{\,2}_{nlj}(r)[m/\bar{m}(r,E_{nlj})]dr\ , \tag{26}$$

with

$$\bar{m}/m(r,E_{nlj})=1-[m^*_{\rm HF}/m(r,E_{nlj})]^{-1}\frac{d}{dE}\times\Delta V(r,E_{nlj})\ .$$

Our S_{nlj} values calculated for $E<0$ are listed in Table IV and shown in Fig. 9 (bottom panel). These values should be compared with absolute spectroscopic factors which in principle can be obtained from $(e,e'p)$ measurements.[47] Very recently, such data became available for the $1d_{3/2}$ and $2s_{1/2}$ orbits[42] (fourth column of Table IV). As can be seen, these values are in better agreement with our results than with those extracted from the proton transfer reactions ^{40}Ca$(\tau,d)^{41}$Sc and ^{40}Ca$(d,\tau)^{39}$K. The corresponding numerical values were taken from Table

TABLE IV. Absolute spectroscopic factor of proton single-particle states in ^{40}Ca.

nlj	S_{nlj} Present work	Ref. 12	$(e,e'p)$ Ref. 42	Nucleon transfer Ref. 48
$1f_{7/2}$	0.72	0.73		1.20
$1d_{3/2}$	0.70	0.73	0.65	0.99
$2s_{1/2}$	0.70	0.79	0.51	0.88
$1d_{5/2}$	0.72	0.74		0.77
$1p_{1/2}$	0.90	1.03		
$1p_{3/2}$	0.87	1.08		
$1s_{1/2}$	0.83	1.07		

IX of Ref. 48. However, the low value found in Ref. 42 for the $2s_{1/2}$ state is not confirmed by our analysis. To our knowledge, experimentally determined strength information about the deeply bound single-particle states is not available.

The spectroscopic factors obtained in Ref. 12 are in general larger than our results. This follows mainly from the different definitions used here and in Ref. 12 for calculating S_{nlj}. As pointed out by Mahaux and Sartor,[16] Eq. (26) yields values for S_{nlj} which are about 10% smaller than those calculated from Eq. (7.6) of Ref. 12.

5. *Spectral functions*

Spectral functions can be defined [4,16] in the context of the DOMA and IMA studies. According to Eq. (8.11) of Ref. 16, which gives a corrected version of Eq. (12.5) used in Ref. 4, the spectral function of a single-particle state is defined as

$$\mathcal{S}_{nlj}(E)=-\pi^{-1}\frac{S_{nlj}\mathcal{W}_{nlj}(E)/(m^*_{nlj}/m)}{(E-E_{nlj})^2+[\mathcal{W}_{nlj}(E)/(m^*_{nlj}/m)]^2}\ , \tag{27}$$

where S_{nlj} represents the absolute spectroscopic factor, Eq. (26), (m^*_{nlj}/m) the expectation value of the effective mass m^*/m, Eq. (20), and $\mathcal{W}_{nlj}(E)$ the expectation value of the imaginary part of the mean field.

Spectral functions were calculated for the $1d_{5/2}$, $1p_{1/2}$, $1p_{3/2}$, and $1s_{1/2}$ proton hole states in ^{40}Ca. These individual spectral functions (multiplied by $2j+1$) together with their weighted sum, as defined by

$$\mathcal{S}_n(E)=\sum_{nlj}(2j+1)\mathcal{S}_{nlj}(E)\ , \tag{28}$$

are presented in Fig. 10. Our calculated distributions of single-particle strength, especially the widths of the $1s_{1/2}$ and $1p$ states, are in good agreement with results obtained from $(e,e'p)$ experiments.[44,45] It is obvious from Fig. 10 that a substantial amount of the $1d_{5/2}$ strength is located at quite high excitation energies (see dotted curve). This comment also applies for the other hole states. In fact, even at −70 MeV the total single-particle strength is quite substantial and about 10% of the integrated total strength is located beyond that energy.

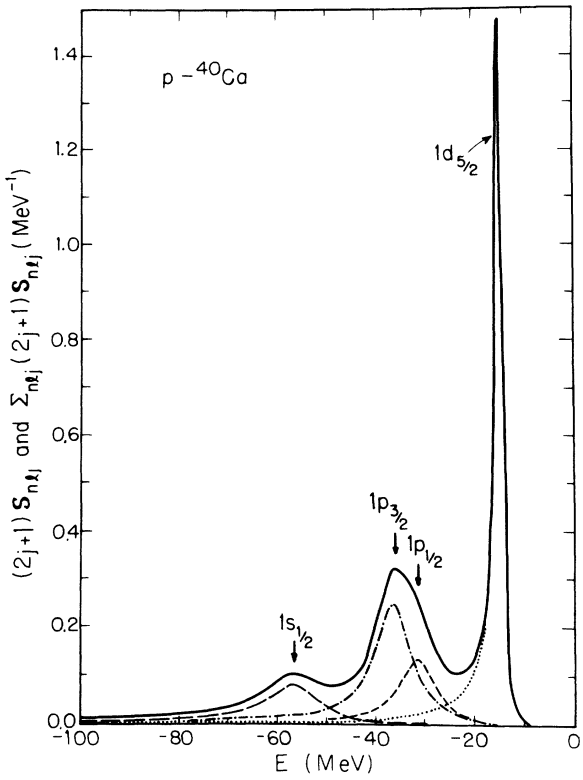

FIG. 10. Proton-hole spectral functions as defined by Eq. (27). The solid curve represents the weighted sum of the $1d_{5/2}$, $1p_{1/2}$, $1p_{3/2}$, and $1s_{1/2}$ proton holes in ^{40}Ca [Eq. (28)]. The dotted curve shows the tail of the $1d_{5/2}$ spectral function. The short-dashed curve represents the $1p_{1/2}$ spectral function. The dashed-dotted curve shows the contribution of the $1p_{3/2}$ spectral function. Finally, the long-dashed curve displays the $1s_{1/2}$ spectral function.

C. Quasibound orbits

Due to the centrifugal and Coulomb barriers, quasibound proton s.p. states exist in ^{40}Ca at positive energies. In Table V we present the calculated energy, root-mean-square radius, occupation probability, and spectroscopic factor for the quasibound s.p. states predicted by our model.

(i) Radii. The associated proton s.p. wave functions were calculated with the boundary condition that they vanish at $R=8.2$ fm, which is twice the radius of our Hartree-Fock potential. Except for $R^{\rm rms}_{nlj}$, the calculated quantities do not heavily depend on the choice of cutoff radius. Our $R^{\rm rms}_{nlj}$ values (see the third column) are given only to illustrate that they closely follow the pattern found in Ref. 4 for the corresponding, however bound,

TABLE V. Energy, root-mean-square radius, occupation probability, and absolute spectroscopic factor for quasibound proton single-particle orbits in ^{40}Ca.

		$R^{\rm rms}_{nlj}$ (fm)			S_{nlj}		
nlj	E_{nlj} (MeV)	Present results	Ref. 12	N_{nlj}	Present results	Ref. 12	Refs.49–51
$1g_{7/2}$	+21.0	5.16		0.04	1.11		
$1g_{9/2}$	+9.75	5.30		0.06	1.00		
$1f_{5/2}$	+4.51	5.16	4.14	0.08	0.76	0.93	0.77
$2p_{1/2}$	+2.02	5.44	4.12	0.07	0.81	0.87	0.83
$2p_{3/2}$	+0.92	4.96	4.09	0.08	0.79	0.84	0.94

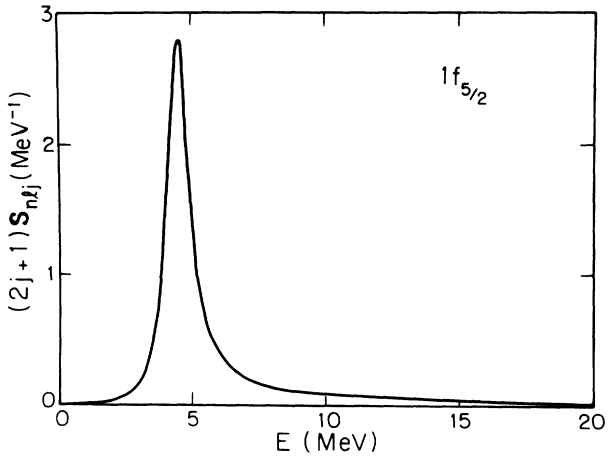

FIG. 11. Spectral function for the $1f_{5/2}$ quasibound proton single-particle state in ^{40}Ca.

neutron $2p_{3/2}$, $2p_{1/2}$, and $1f_{5/2}$ s.p. orbits in ^{40}Ca. As already observed for the bound s.p. orbits, the radii of unbound orbitals given in Ref. 12 are quite different from our results.

(ii) Occupancies. Our predicted occupation probabilities N_{nlj} are smaller than 0.1.

(iii) Spectroscopic factors and spectral functions. The calculated absolute spectroscopic factors S_{nlj} for the $2p_{3/2}$, $2p_{1/2}$, and $1f_{5/2}$ orbits take on values $S_{nlj} \sim 0.8$ which, except for the $2p_{3/2}$ state, compare very well with the experimental values (i.e., 0.77 and 0.83) inferred from proton transfer reactions and elastic proton scattering on ^{40}Ca (Refs. 49–51). This agreement is fortuitous, however. To illustrate this statement, Fig. 11 presents the calculated spectral function for the $1f_{5/2}$ state. The energy range covered by experiments extends up to only 7.12 MeV. From Fig. 11 it can be seen that more than 20% of the calculated $1f_{5/2}$ strength is located above that energy. Therefore, an experimental value near 0.62 rather than 0.77 would be in better agreement with our result of 0.76 obtained for the entire excitation energy range. Detailed experimental information about the $1g_{9/2}$ state is not available. Since we find this quasibound s.p. state located at +9.75 MeV, it is not surprising that in Refs. 49–51 only less than 25% of the expected strength could be identified at energies lower than 7.12 MeV. According to our analysis, the $1g_{7/2}$ orbit is also quasibound. The calculated distribution of quasibound single-particle strength and its weighted sum [Eq. (28)] are shown in Fig. 12.

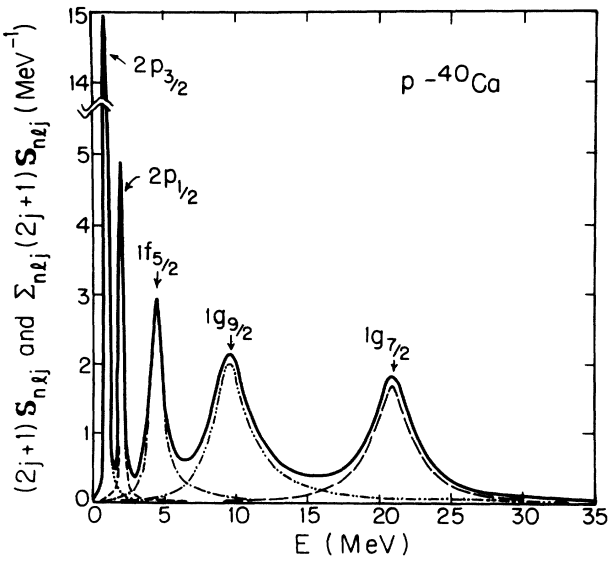

FIG. 12. Individual spectral functions of quasibound proton orbits calculated from Eq. (27) and their weighted sum [Eq. (28), solid curve].

For completeness, the S_{nlj} values obtained in Ref. 12 are listed for some unbound orbits. After renormalization (see Sec. III B 4) the spectroscopic factors for the $2p$ proton s.p. orbits agree very well with the present predictions, while the $S_{1f_{5/2}}$ value of Ref. 12 is considerably larger than our result.

D. Comparison between ^{40}Ca and ^{208}Pb

At this stage, it is interesting to compare the s.p. properties of ^{40}Ca with those for ^{208}Pb since a wealth of data exists for these spherical nuclei that are widely considered as testing grounds in nuclear structure studies. The main striking feature which emerges from this comparison is that the 15% depletion of the Fermi sea predicted for ^{40}Ca is considerably weaker than that found in the lead region. There, the $3s_{1/2}$ proton orbit (hole state closest to Fermi energy) displays an occupancy of 0.7 or less, as deduced from either calculations or measurements.[52,53]

Part of the deviation observed between the predictions stems from different treatments of correlations in ground states. In Ref. 52, short-range and tensor correlations are explicitly considered while the DOMA includes these correlations and others in a global and implicit manner. Therefore, our phenomenological results suggest that the microscopic calculations of Ref. 52 overpredict the depletion of the Fermi sea, a conclusion that is also supported by recent $(\vec{d},p)$ measurements on ^{40}Ca.[54]

On the other hand, our predicted depletion for ^{40}Ca is consistent with recent experimental results obtained for ^{208}Pb and adjacent nuclei. First, Grabmayr *et al.*[55] have deduced a 12% depletion of the Fermi sea in ^{208}Pb from a sophisticated, joint analysis of nucleon transfer and electron scattering experiments. This result compares well with our 15% predicted depletion for ^{40}Ca. Second, our results agree very well with new electron scattering data[56] on the magnetic form factors of ^{205}Tl and ^{207}Pb. In these experiments, the quantity $Z = n_- - n_+$, with n_+ and n_- as the occupation probability of orbitals lying immediately above and below the Fermi energy, was found to be equal to 0.70 ± 0.07. This figure is to be compared with $Z = 0.71$ that is predicted for ^{40}Ca.

Obviously, this comparison between ^{40}Ca and ^{208}Pb is far from complete. More measurements on both nuclei

are needed before a more precise statement as to whether the Fermi seas in both nuclei are depleted by comparable amounts can be made.

Finally, recent theoretical calculations[57] performed in normal nuclear matter indicate a 13% depletion originating from short-range correlations. This result would be consistent with our phenomenological estimate if the effects of the long-range correlations on the whole depletion were to be a few percent in magnitude.

IV. DISCUSSION

So far, our study has mostly dealt with the determination of the p-^{40}Ca mean field from a dispersive optical-model analysis approach. This mean field displays global properties which are now compared with those established earlier for the same system from an iterative moment approach.[12] The global parameters of interest are (i) volume integral per nucleon

$$(J/A)_{\mathcal{V}}=\frac{4\pi}{A}\int r^2\mathcal{V}(r,E)dr\ ,$$

(ii) root-mean square (rms) radius

$$R^{\mathcal{V}}_{\rm rms}=\frac{[\int r^4\mathcal{V}(r,E)dr]^{1/2}}{[\int r^2\mathcal{V}(r,E)dr]^{1/2}} \tag{29}$$

of the full dispersive potential $\mathcal{V}(r,E)$, as well as

$$J_{\mathcal{W}}/A=\frac{4\pi}{A}\int r^2\mathcal{W}(r,E)dr$$

of the full absorptive potential $\mathcal{W}(r,E)$.

The variations of $J_{\mathcal{V}}/A$ and $R^{\mathcal{V}}_{\rm rms}$ with energy are shown in Fig. 13. Here the solid and dot-dashed curves are for the DOMA and IMA results, respectively. Figure 13 also includes the volume integral $(J/A)_{\mathcal{V}_{\rm HF}}$ and rms radius $R^{\rm HF}_{\rm rms}$ of the empirical Hartree-Fock potential. These parameters are shown as dashed and dotted curves depending upon whether they are obtained from DOMA and IMA. As can be seen in Fig. 13, the HF component of (J/A) as deduced from DOMA has a stronger E dependence than that found from IMA. Part of this difference can be traced back to the fact that the two methods are quite different in nature. In contrast, the $(J/A)_{\mathcal{V}}$ values from DOMA and IMA differ by only 3% or less at positive energies ranging from 20 to 75 MeV where experimental information on scattering and reaction processes are available. This comparison indicates that the volume integral of the real part of the full mean field is determined within an uncertainty of better than 2% at positive energies. At negative energies, this uncertainty seems to be much larger. This can be seen in Fig. 13 where the relative difference between the $(J/A)_{\mathcal{V}}$'s from DOMA and IMA is as large as 10% at the Fermi energy. At this stage, we do not completely understand the origin of this difference, since DOMA and IMA both lead to similar predictions for particle- and hole-state energies. On the other hand, the difference observed in Fig. 13 for the E dependence of the $(J/A)_{\mathcal{V}}$'s can be traced back to the assumptions made for the absorption at

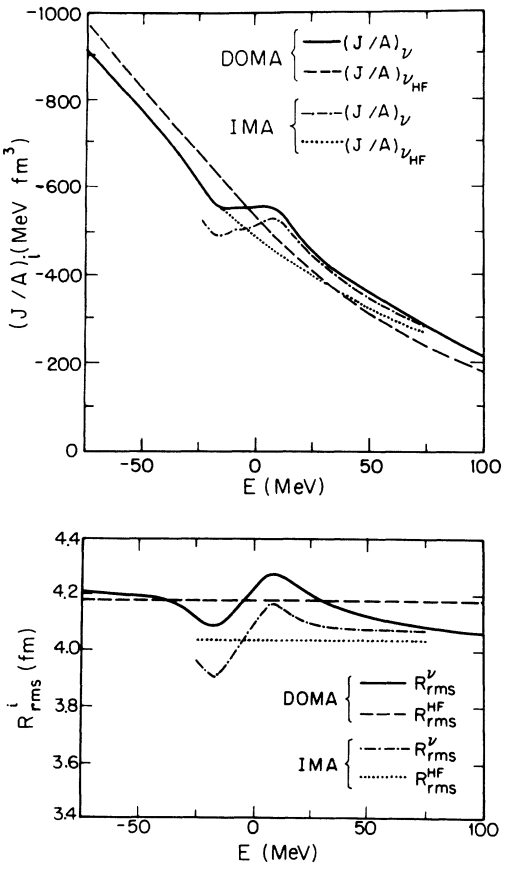

FIG. 13. Top panel: Energy dependence of the volume integral per nucleon of the full real potential (solid curve) and of its Harteee-Fock component (dashed curve) as obtained from the present DOMA. The corresponding iterative moment approach (IMA) results of Ref. 12 are given by the dashed-dotted and dotted curves, respectively. Bottom panel: Energy dependence of the root-mean-square radius [see Eq. (29)] of the full real potential (solid curve) and its Hartree-Fock component (dashed curve) as calculated from the DOMA. The corresponding IMA results of Ref. 12 are represented by the dashed-dotted and dotted curves, respectively.

higher energies. This is illustrated in Fig. 14, which displays the volume integrals $(J/A)_{\mathcal{W}}$ from DOMA and IMA. As can be seen, $(J/A)_{\mathcal{W}}$ reaches an asymptotic regime at lower energies in IMA (see curves labeled as BR and JM which were taken from Ref. 12) than it does in DOMA.

The features found for the $(J/A)_{\mathcal{W}}$ values and E dependences may also explain why the rms radii $R^{\mathcal{W}}_{\rm rms}$ deduced from DOMA and IMA do not display the same variations with energy (see bottom part of Fig. 13). From this figure, it can be seen that $R^{\mathcal{V}}_{\rm rms}$(DOMA) $> R^{\mathcal{V}}_{\rm rms}$(IMA) for $E<75$ MeV. This stems from the fact that the Hartree-Fock radius was found to be larger in DOMA (i.e., $r_{\rm HF}=1.20$ fm) than in IMA (i.e., $r_{\rm HF}=1.13$ fm). On the other hand, $R^{\mathcal{V}}_{\rm rms}$(DOMA) and $R^{\mathcal{V}}_{\rm rms}$(IMA) display similar patterns around $E=E_F$.

Finally, we have constructed a Woods-Saxon shape that is equivalent to the real parts of the full mean field.

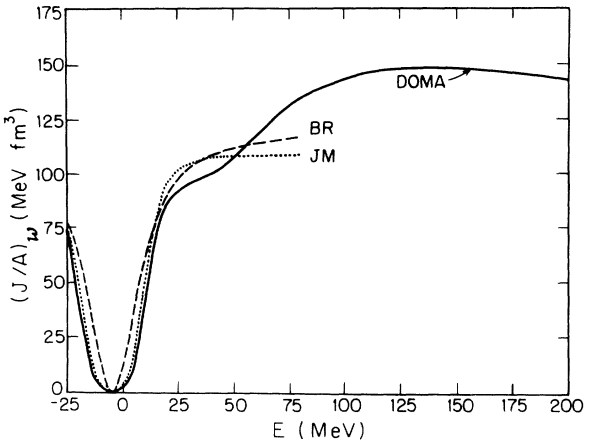

FIG. 14. Energy dependence of the volume integral per nucleon of the full absorptive potential $\mathcal{W}$ as obtained in the DOMA (solid curve) and in the IMA with the Jeukenne-Mahaux (JM) form factor (dotted curve) and the Brown-Rho (BR) form factor (dashed curve).

This has been achieved from an identification of their respective volume integrals and rms radii. Assuming that the diffuseness $\tilde{a}_V$ of the equivalent WS shape is constant and equal to 0.73 fm [i.e., $\tilde{a}_V \equiv a_V$, with a_V as the diffuseness of the volume potential defined in Eq. (2)], then $\tilde{r}_V$, the equivalent radius, takes on values that vary smoothly with energy as shown in Fig. 15. At the Fermi energy, $\tilde{r}_V$ (solid curve) is equal to the HF radius (dashed curve). The equivalent radius reached a maximum value $\tilde{r}_V = 1.25$ fm at $E = 10$ MeV and then decreases smoothly. At $E = 100$ MeV, its value is $\tilde{r}_V = 1.14$ fm.

V. CONCLUSION

In this work, the DOMA of Mahaux and Ngô was used to construct the proton mean field in ^{40}Ca. This method, which previously was employed in neutron mean-field studies turned out to be very successful for the p-^{40}Ca system as well. The proton interaction in this closed-shell nucleus has been determined from -60 MeV up to $+200$ MeV. The predictions based on the mean field are in good agreement with both bound-state and scattering properties measured over this broad energy range. In particular, the $\sigma(\theta)$ $A_y(\theta)$ measurements at 182 MeV are rather well reproduced. This energy is at the edge of the intermediate energy region where Dirac phenomenology and Brueckner-Hartree-Fock theory are usually used to describe the complex scattering potential. The quality of the fits obtained at 182 MeV indicates that the DOMA approach might be another proper tool for describing elastic scattering up to 200 MeV.

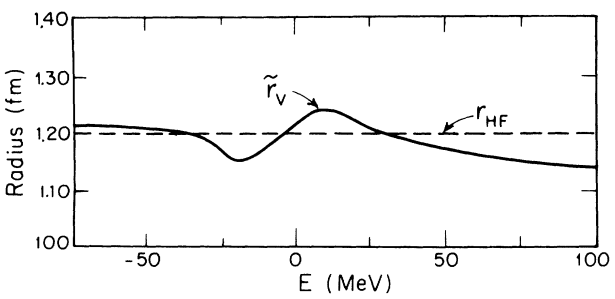

FIG. 15. Energy dependence of the radius parameter $\tilde{r}_V$ of the real full potential well which was parametrized by an equivalent Woods-Saxon potential. For comparison, the radius parameter r_{HF} of the Hartree-Fock component is also shown.

In keeping with Brieva and Rock and Dirac phenomenology, no significant amount of imaginary spin-orbit strength was needed to fit the $A_y(\theta)$ data below 80 MeV. Therefore, it seems reasonable to state that the amount of W_{SO} strength previously required to fit $(\mathbf{n},n)$ and $(\mathbf{p},p)$ scattering data below 50 MeV with standard potential form factors is an artifact which results from ignoring the dispersive terms, especially $\Delta\mathcal{V}_D(r,E)$, in the n-^{40}Ca and p-^{40}Ca mean fields.

The p-^{40}Ca system is of special interest in mean-field studies since the location of the deeply bound $1p$ and $1s$ proton orbits is known from $(e,e'p)$ experiments. This knowledge places severe constraints on the energy dependence of the Hartree-Fock component of the mean field. As a result, a linear energy dependence is required at negative energies in contrast to the exponential energy dependence observed at positive energies. It was found that an exponential energy dependence of $V_{HF}(E)$ would substantially overbind the deeply bound proton hole states.

Our predicted root-mean-square radii of the proton s.p. orbits in ^{40}Ca can serve as a benchmark for testing the accuracy of the DOMA approach. Electron scattering experiments offer an elegant technique to determine such radii. The DOMA approach predicts s.p. occupation probabilities which are depleted by 15% at the Fermi energy, a feature at variance with the traditional shell-model picture. It is the existence of the imaginary component of the mean field that causes the calculated values for the occupation probability to be larger than zero for particle states and smaller than unity for hole states. Although our analysis is in agreement with theoretical expectations[53] for the occupancy of particle states near the Fermi energy, i.e., $N_{nlj} \lesssim 0.1$ (see Fig. 9, top panel), our calculated depletion of the Fermi sea for protons is only half of that predicted in Ref. 53. Recent studies for neutrons in ^{40}Ca also rule out a depletion of 20% or more.[4,54]

The calculated spectral functions clearly demonstrate that for s.p. orbits further away from the Fermi energy, a substantial amount of strength is located at quite high excitation energy. Therefore, it is not surprising that S_{nlj} values derived from data obtained in a limited energy range cannot account for the full strength. It would be interesting to have accurate, experimental spectral functions available in order to compare with our predictions, especially for the deeply bound s.p. states.

ACKNOWLEDGMENTS

The authors wish to express their gratitude to Dr. C. H. Johnson for stimulating discussions and for providing a code used to calculate single-particle bound-state energies. We thank Dr. A. Thiel for calculating the wave functions for the quasibound proton single-particle orbits in ^{40}Ca and Dr. R. K. Das for his assistance in the calculations of occupation probabilities and spectroscopic factors. One of us (J.P.D.) acknowledges the hospitality and support of Triangle Universities Nuclear Laboratory during part of this study. This work was supported in part by the U.S. Department of Energy, Office of High Energy and Nuclear Physics, under Contract No. DE-AC05-76ER01067.

---

*Permanent address: Tsinghua University, Beijing, The People's Republic of China.

[1]C. Mahaux and H. Ngô, Nucl. Phys. **A378**, 205 (1982).
[2]J. P. Delaroche and W. Tornow, Phys. Lett. B **203**, 4 (1988).
[3]W. Tornow and J. P. Delaroche, Phys. Lett. B **210**, 26 (1988).
[4]C. H. Johnson and C. Mahaux, Phys. Rev. C **38**, 2589 (1988).
[5]R. D. Lawson, P. T. Guenther, and A. B. Smith, Nucl. Phys. **A493**, 267 (1989).
[6]C. H. Johnson, R. F. Carlton, and R. R. Winters, Phys. Rev. C **39**, 415 (1989).
[7]J. P. Delaroche, Y. Wang, and J. Rapaport, Phys. Rev. C **39**, 391 (1989).
[8]A. B. Smith, P. T. Guenther, and R. D. Lawson, Nucl. Phys. **A455**, 344 (1986).
[9]C. H. Johnson, D. J. Horen, and C. Mahaux, Phys. Rev. C **36**, 2252 (1987); J. P. Jeukenne, C. H. Johnson, and C. Mahaux, *ibid.* **38**, 2573 (1988).
[10]R. W. Finlay, J. Wierzbicki, and R. K. Das, Phys. Rev. C **39**, 804 (1989).
[11]R. D. Lawson, P. T. Guenther, and A. B. Smith, Phys. Rev. C **36**, 1298 (1987); R. K. Das, R. W. Finlay, J. Wierzbicki, and F. S. Dietrich, Bull. Am. Phys. Soc. **33**, 1567 (1988).
[12]C. Mahaux and R. Sartor, Nucl. Phys. **A484**, 205 (1988), and references therein.
[13]C. Mahaux and R. Sartor, Phys. Rev. C **36**, 1777 (1987).
[14]C. Mahaux and R. Sartor, Nucl. Phys. **A475**, 247 (1987); **A468**, 193 (1987), and references therein.
[15]C. Mahaux and R. Sartor, Nucl. Phys. **A481**, 381 (1988); **A481**, 407 (1988).
[16]C. Mahaux and R. Sartor, Nucl. Phys. **A493**, 157 (1989); **A503**, 525 (1989).
[17]G. M. Honoré, W. Tornow, C. R. Howell, R. S. Pedroni, R. C. Byrd, R. L. Walter, and J. P. Delaroche, Phys. Rev. C **33**, 1129 (1986), and references therin.
[18]E. T. Boschitz, R. W. Bercaw, and J. S. Vincent, Phys. Lett. **13**, 322 (1964).
[19]K. H. Bray, K. S. Jayaraman, G. A. Moss, W. T. H. van Oers, D. O. Well, and Y. I. Wu, Nucl. Phys. **A167**, 57 (1971).
[20]D. L. Watson, J. Lowe, J. C. Dove, R. M. Craig, and D. J. Baugh, Nucl. Phys. **A92**, 193 (1967).
[21]B. W. Ridley and J. F. Turner, Nucl. Phys. **58**, 497 (1964).
[22]V. Hnizdo, O. Karban, J. Lowe, G. W. Greenlees, and W. Makofske, Phys. Rev. C **3**, 1560 (1971).
[23]C. R. Gruhn, T. Y. T. Kuo, C. J. Maggiore, H. McManus, F. Petrovich, and B. M. Preedom, Phys. Rev. C **6**, 915 (1972).
[24]L. N. Blumberg, E. E. Gross, A. van der Woude, A. Zucker, and R. H. Bassel, Phys. Rev. **147**, 812 (1966).
[25]E. E. Gross, R. H. Bassel, L. N. Blumberg B. J. Morton, Z. van der Woude, and A. Zucker, Nucl. Phys. **A102**, 673 (1967).
[26]R. M. Craig, J. C. Dove, J. Lower, and D. L. Watson, Nucl. Phys. **86**, 113 (1966).
[27]C. B. Fulmer, J. B. Ball, A. Scott, and L. Whiten, Phys. Rev. **181**, 1565 (1969).
[28]H. Sakaguchi, M. Nakamura, K. Hatanaka, A. Goto, T. Noro, F. Ohtani, H. Sakamoto, H. Ogawa, and S. Kobayashi, Phys. Rev. C **26**, 944 (1982).
[29]H. Sakaguchi, M. Yosoi, M. Nakamura, T. Noro, H. Sakamoto, T. Ichihara, M. Ieiri, Y. Takeuchi, H. Togawa, T. Tsutsumi, and S. Kobayashi, J. Phys. Soc. Jpn. Suppl. **55**, 61 (1986).
[30]P. Schwandt, H. O. Meyer, W. W. Jacobs, A. D. Bacher, S. E. Vigdor, M. D. Kaitchuck, and T. R. Donoghue, Phys. Rev. C **26**, 55 (1982).
[31]A. Nadasen, P. Schwandt, P. P. Singh, W. W. Jacobs, A. D. Bacher, P. T. Debevec, M. D. Kaitchuck, and J. T. Meek, Phys. Rev. C **23**, 1023 (1981).
[32]W. Bauhoff, At. Data Nucl. Data Tables **35**, 429 (1986), and references therein.
[33]W. T. H. van Oers, Phys. Rev. C **3**, 1550 (1971).
[34]B. C. Clark, S. Hama, and R. L. Mercer, in *The Interaction Between Medium Energy Nucleons in Nuclei (Indiana Cyclotron Facility, Bloomington, Indiana, 1982)*, Proceedings of the Interaction Between Medium Energy Nucleons in Nuclei, AIP Conf. Proc. No. 97, edited by H. O. Meyer (AIP, New York, 1982), p. 260.
[35]J. P. Jeukenne and C. Mahaux, Nucl. Phys. **A394**, 445 (1983).
[36]J. S. Winfield, Sam M. Austin, R. P. De Vito, U. E. P. Berg, Ziping Chen, and W. Sterrenberg, Phys. Rev. C **33**, 1 (1986).
[37]E. Hagberg, A. Ingemarsson, and B. Sundqvist, Phys. Scr. **3**, 245 (1971); A. Ingemarsson and G. Tibbell, *ibid.* **4**, 235 (1971).
[38]E. D. Cooper, Nucl. Phys. **A495**, 483 (1989).
[39]F. A. Brieva and J. R. Rook, Nucl. Phys. **A307**, 493 (1978).
[40]P. Schwandt, in *The Interaction Between Medium Energy Nucleons in Nuclei, 1982* (Ref. 34), p. 89.
[41]V. A. Madsen and F. Osterfeld, Phys. Rev. C **39**, 1215 (1989).
[42]G. J. Kramer, H. P. Blok, J. F. J. van den Brand, H. J. Bulten, R. Ent, E. Jans, J. B. J. M. Lanen, L. Lapikas, H. Nann, E. N. M. Quint, G. van der Steenhoven, P. K. A. de Witt Huberts, and G. J. Wagner, Phys. Lett. B **227**, 199 (1989).
[43]C. Mahaux and H. Ngô, Nucl. Phys. **A431**, 486 (1984).
[44]K. Nakamura, S. Hiramatsu, T. Kamae, H. Muramatsu, N. Izutsu, and Y. Watase, Nucl. Phys. **A271**, 221 (1976).
[45]J. Mougey, M. Bernheim, A. Bussière, A. Gillebert, Phan Xuan Hô, M. Priou, D. Royer, I. Sick, and G. J. Wagner, Nucl. Phys. **A262**, 461 (1976); S. Frullani and J. Mougey, in *Advances in Nuclear Physics*, edited by J. W. Negele and E. Vogt (Plenum, New York, 1984), Vol. 14, p. 1.
[46]G. Landaud, J. Yonnet, S. Kullander, F. Lemeilleur, P. U. Renberg, B. Fagerström, A. Johansson, and G. Tibell, Nucl. Phys. **A173**, 337 (1971); S. Kullander, F. Lemeilleur, P. U. Renberg, G. Landaud, J. Yonnet, B. Fagerström, A. Johansson, and G. Tibell, *ibid.* **A173**, 357 (1971).

[47]A. E. L. Dieperink and I. Sick, Phys. Lett. **108B**, 1 (1982).
[48]P. Doll, G. J. Wagner, K. T. Knöpfle, and G. Mairle, Nucl. Phys. **A263**, 210 (1976).
[49]D. H. Youngblood, R. L. Kozub, R. A. Kenefick, and J. C. Hiebert, Phys. Rev. C **2**, 477 (1970).
[50]A. Marinov, C. Drory, E. Navon, J. Burde, and G. Engler, Phys. Rev. Lett. **23**, 23 (1969).
[51]W. F. Rich, Ph.D. thesis, Rice University, 1967 (unpublished).
[52]S. Fantoni and V. R. Pandharipande, Nucl. Phys. **A427**, 473 (1984), and references therein.
[53]V. R. Pandharipande, C. N. Papanicolas, and J. Wambach, Phys. Rev. Lett. **53**, 1133 (1984).
[54]F. J. Eckle, H. Lenske, G. Eckle, G. Graw, R. Hertenberger, H. Kader, F. Merz, H. Nann, P. Schiemenz, and H. H. Wolter, Phys. Rev. C **39**, 1662 (1989); F. J. Eckle, H. Lenske, G. Eckle, G. Graw, R. Hertenberger, H. Kader, H. J. Maier, F. Metz, H. Nann, P. Schiemenz, and H. H. Wolter, Nucl. Phys. **A506**, 159 (1990).
[55]P. Grabmayr, G. J. Wagner, H. Clement, and R. Röhm, Nucl. Phys. **A494**, 244 (1989).
[56]C. N. Papanicolas, L. S. Cardman, J. H. Heisenberg, O. Schwentker, T. E. Milliman, F. W. Hersman, R. S. Hicks, G. A. Peterson, J. S. McCarthy, J. Wise, and B. Frois, Phys. Rev. Lett. **58**, 2296 (1987).
[57]A. Ramos, A. Polls, and W. H. Dickhoff, Nucl. Phys. **A503**, 1 (1989).